Nigerian Journal of Physics (NJP)
ISSN online: 3027-0936
ISSN print: 1595-0611
DOI: https://doi.org/10.62292/njp.v34i3.2025.425
Volume 34(3), September 2025

Unconstrained 3D Inversion of Airborne Magnetic Data for Mineral Targeting in the Southwestern Nigerian Basement Complex

*[1]Ohaegbuchu, H. E., [1]Dinneya, O. C., [1]Nwokoma, E. U., [1]Uzoaru, S. I. and [2]Musa, Y. A.

[1]Department of Physics, Michael Okpara University of Agriculture, Umudike. Abia State.
[2]Department of Physics, Bayero University, Kano State, Nigeria.

*Corresponding Author's Email: eo.henry@mouau.edu.ng Phone: +2348132954367

ABSTRACT

This study applies unconstrained 3D inversion of high-resolution airborne magnetic data to model subsurface susceptibility distribution in the Southwestern Basement Complex of Nigeria. Total magnetic intensity (TMI) data were processed to residual magnetic anomalies, first vertical derivative (FVD), and analytical signal maps, followed by inversion using GM-SYS 3D in Oasis Montaj software (cell size: 250 × 250 × 100 m). The model converged after 50 iterations, achieving an RMS misfit of $11.8\,nT$ and $R^2 = 0.927$. High-susceptibility anomalies (>0.05 cgs) extend laterally over 5–20 km and to depths exceeding 1.5 km, aligning with major NE–SW and NW–SE structural corridors. Integration of magnetic depth estimates, structural trends, and inversion results highlights prospective targets for iron oxide–copper–gold (IOCG), skarn-type, and gold-bearing systems. These targets coincide with structurally complex zones near the boundaries of high and low magnetic domains. The results provide a framework for prioritizing mineral exploration in the region.

Keywords:
3D Magnetic Inversion,
Mineral Exploration,
Nigerian Basement Complex,
Magnetic Susceptibility,
Airborne Geophysics.

INTRODUCTION

The Nigerian Basement Complex forms part of the Pan-African mobile belt, which evolved during Neoproterozoic orogenic events (~750–550 Ma) and comprises high-grade metamorphic and igneous rocks including schists, gneisses, migmatites, and syn- to post-tectonic granitoids (Rahaman, 1988; Odeyemi, 1990; Adegbuyi et al., 2021; Salawu & Oden, 2022). These lithologies have undergone multiple deformation episodes characterized by brittle-ductile shearing, faulting, and extensive hydrothermal alteration, creating favorable conditions for ore deposit formation (Rahaman, 1988; Abubakar, Yakubu, & Ajayi, 2023).

The study area's proximity to the Middle Benue Trough, a major intracontinental rift system, enhances its mineral prospectivity through the superposition of basement structures, magmatic activity, and regional tectonics. Previous investigations have documented significant mineralization, including gold occurrences at Iperindo and Ilesha, lead–zinc deposits in the Abakaliki area, and iron formations throughout the basement terrain (Udensi & Osazuwa, 2004; Anudu et al., 2014; Adegbuyi et al., 2021; Salawu & Oden, 2022). The primary aim of this study is to apply unconstrained 3D magnetic inversion for the accurate delineation of subsurface geological architecture and identification of mineralization potential within the study area.

Unconstrained 3D Inversion Approach

Unconstrained 3D magnetic inversion offers notable advantages by minimizing prior assumptions and allowing magnetic susceptibility distributions to emerge directly from the data (Li & Oldenburg, 1996, 1998). This methodology accommodates geological complexity and enables more objective subsurface imaging. Utsugi (2021) extends this by introducing a sparse regularization scheme with L1 norm and total-variation penalties in magnetic inversion, which results in sharply focused, block-like structures—thereby increasing clarity and reducing inversion ambiguity.

Geological Setting

Regional Geology

The study area lies within the southwestern portion of the Nigerian Basement Complex, bounded by longitudes 7.5°–8.5°E and latitudes 6.0°–7.0°N, encompassing approximately 12,100 km². The Precambrian underlies the region, followed by early Paleozoic crystalline rocks that underwent polyphase deformation and metamorphism during the Pan-African orogeny.

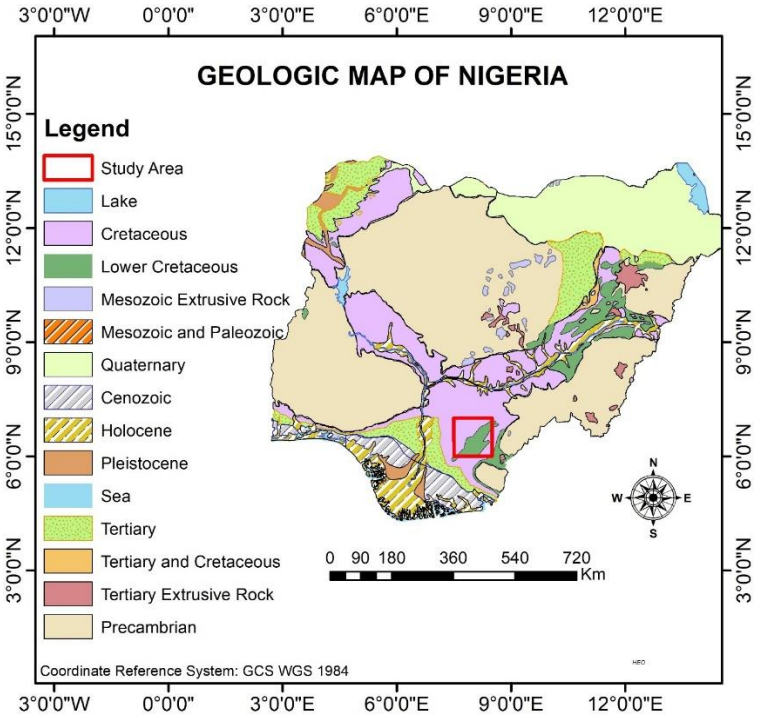

Figure 1: Geologic Map of Nigeria Showing the Study Area of Interest

The Nigerian Basement Complex is considered the northernmost extension of the Congo Craton and was significantly reactivated during the Pan-African tectonic event (Ajibade et al., 2008; Oyinloye, 2011). It comprises several lithostratigraphic units, including the Migmatite–Gneiss Complex, with protolith ages exceeding 2000 Ma, the Schist Belts, which formed between approximately 750 and 600 Ma, and the Older Granites, dated to between 610 and 580 Ma (Rahaman, 1988; Dada, 2006). These units are intruded by the Younger Granites of the Jos Plateau, emplaced around 170 Ma (Bowden et al., 1987).

Lithological Units

The study area is underlain by a range of lithological units reflecting a complex geological evolution, with the dominant rock types summarized as follows:

Migmatitic Gneisses represent the oldest lithologies, characterized by alternating felsic and mafic bands formed under high-grade metamorphic conditions involving partial melting. These units are often the hosts of gold mineralization, particularly along shear zones and within quartz veins. Structurally, the gneisses display intricate foliation patterns indicative of multiple deformation phases. Mineral assemblages including garnet, sillimanite, and cordierite suggest metamorphic conditions ranging from upper amphibolite to granulite facies (Ema et al., 2024; Yakubu et al., 2023).

Schists comprise medium-grade metasedimentary rocks, such as biotite, muscovite, and garnet-bearing schists. These units commonly contain disseminated sulfides and graphite, which influence their magnetic properties. The schist belts are interpreted as supracrustal sequences that were originally deposited in volcano-sedimentary basins and subsequently metamorphosed during the Pan-African orogenic cycle (Olawale et al., 2023).

Granitoids consist of Pan-African intrusive bodies, ranging in composition from granite to granodiorite, emplaced between 750 and 550 Ma. These intrusions are spatially and genetically associated with tin, tungsten, and rare earth element (REE) mineralization. Geochemically, the granitoids exhibit calc-alkaline to high-K calc-alkaline signatures, consistent with a subduction-related magmatic origin (Odeyemi & Ibrahim, 2024).

Mafic to Ultramafic Bodies occur as small-scale intrusions including amphibolites, pyroxenites, and serpentinites. These lithologies are notable for their elevated magnetic susceptibilities and are considered prospective for nickel, copper, and platinum group element (Ni-Cu-PGE) mineralization. Their geological context suggests they may represent remnants of dismembered ophiolite complexes or differentiated layered mafic intrusions (Abraham et al., 2024; Musa et al., 2023).

Structural Framework

The area exhibits complex structural patterns that reflect multiple deformation episodes. Major structural trends include:

i. N-S to NNE-SSW trending shear zones: These represent the dominant structural grain and are

associated with regional-scale strike-slip movement during Pan-African convergence (Yakubu et al., 2023).

ii. E-W fault systems: These structures may represent transform faults or accommodation zones related to regional extension (Olawale et al., 2023).

iii. NW-SE brittle fractures: Late-stage structures possibly related to Cretaceous rifting and formation of the Benue Trough (Odeyemi & Ibrahim, 2024).

These structures serve as important controls on mineralization and fluid migration pathways, with intersection zones being particularly prospective for ore concentration.

Mineralization Context

The region hosts a variety of known mineralization styles, reflecting its complex tectono-metamorphic history and diverse lithological framework. Gold mineralization is predominantly structurally controlled, occurring within quartz veins and shear zones. These deposits are typically found in schist belts and along lithological boundaries, with gold present either as free grains within quartz veins or disseminated in sulfide-rich host rocks (Yakubu et al., 2023).

Iron mineralization is characterized by magnetite-rich layers embedded within metamorphic sequences, particularly in transitional zones between schist belts and surrounding gneissic complexes. These units are interpreted as metamorphosed banded iron formations (BIFs) and exhibit considerable economic potential (Musa et al., 2023).

Base metal occurrences, including lead, zinc, and copper, are largely attributed to hydrothermal activity. This mineralization is commonly found in contact metamorphic environments adjacent to granitic intrusions, suggesting a strong link between magmatic processes and metal transport (Olawale et al., 2023).

Regional Tectonic Evolution

Multiple distinct geodynamic phases characterize the tectonic evolution of the study area. During the Archean to Paleoproterozoic era (>2000 Ma), the foundational basement gneiss complex formed through processes of crustal accretion accompanied by high-grade metamorphism. In the Neoproterozoic period (1000–750 Ma), extensive supracrustal sequences were deposited within intracratonic basins, reflecting a phase of relative tectonic quiescence and basin development. The Pan-African Orogeny (750–550 Ma) marked a major tectonothermal event, involving widespread regional metamorphism, intense deformation, and the emplacement of syn- to post-tectonic granitic intrusions as a result of continental collision (Yakubu et al., 2023; Odeyemi & Ibrahim, 2024). Following this orogenic episode, the region experienced post-collisional extension between 550 and 500 Ma, characterized by lithospheric cooling, uplift, and the development of brittle fault systems. Lastly, during the Mesozoic era (200–100 Ma), the area underwent significant tectonic reactivation linked to the opening of the South Atlantic, culminating in the formation of the Benue Trough and associated magmatic activity (Musa et al., 2023).

MATERIALS AND METHODS

Airborne Magnetic Survey Specifications

The present study area encompasses approximately 12,100 square kilometers within the broader Nigerian Basement Complex, over which a high-resolution airborne magnetic survey was conducted. Data acquisition employed a fixed-wing aircraft equipped with a Geometrics G-823A cesium vapor magnetometer, optimized for high-sensitivity magnetic mapping. The survey design featured a north–south flight line orientation (0°–180°) with 500-meter line spacing, complemented by east–west tie lines spaced at 5000 meters to ensure robust regional control.

The aircraft maintained a nominal altitude of 80 ± 5 meters above ground level, using a radar altimeter to regulate terrain clearance and preserve data consistency. Magnetic measurements were collected at a 0.1-second sampling interval, corresponding to a spatial resolution of approximately 5.1 meters along the flight path. The survey acquired over 18,500 line kilometers of data across the broader region.

Precise navigation was ensured by a differential GPS system offering real-time corrections with a positional accuracy of ±3 meters. A ground-based Geometrics G-856AX proton precession magnetometer served as the base station to monitor and correct for diurnal magnetic variations. The airborne magnetometer's sensitivity of ±0.01 nanotesla (nT) allowed for the detection of subtle magnetic variations, essential for resolving lithological and structural features within the complex geological framework of the basement terrain.

Data Processing and Quality Control

Standard Corrections

The raw magnetic data were subjected to comprehensive preprocessing following standard industry protocols to ensure data quality and interpretability. Diurnal variations were corrected using continuous recordings from a ground-based base station, sampled at 1-second intervals. During the survey period, diurnal corrections ranged from −50 to +45 nanotesla (nT).

The International Geomagnetic Reference Field (IGRF-13), computed for the specific survey epoch, was subsequently subtracted from the diurnally corrected total magnetic intensity data to isolate local anomalies. Altitude corrections were applied to account for variations in flight elevation, utilizing a theoretical magnetic field decay rate of 0.03 nT per meter, appropriate for a monopole source approximation. To

enhance internal consistency, statistical leveling procedures were implemented, including fourth-difference filtering and micro-leveling, which effectively minimized crossover errors at tie-line intersections.

Data Quality Assessment

Quality control analysis confirmed high data integrity across the dataset. Flight line recovery exceeded 99.5%, with only minimal data gaps observed. After leveling procedures, root-mean-square (RMS) tie-line intersection errors were reduced to less than 2 nanotesla (nT), indicating excellent internal consistency. The recorded noise level remained below 0.5 nT under magnetically quiet conditions, while the residual magnetic field exhibited a dynamic range of approximately 420 nT, ensuring sufficient contrast for resolving geological features.

Grid Generation

Data gridding was performed using a minimum curvature interpolation algorithm, optimized to preserve both regional trends and local anomaly shapes. A grid cell size of 125 meters—equivalent to one-quarter of the flight line spacing—was selected to balance resolution and computational efficiency. The interpolation utilized a search radius of 750 meters, corresponding to 1.5 times the line spacing, to ensure adequate spatial coverage. The algorithm was allowed a maximum of 50 iterations, with convergence achieved when changes between iterations fell below a threshold of 1.

Residual Magnetic Anomaly Computation

Regional-residual separation was performed to isolate anomalies from shallow magnetic sources:

$$R(x,y) = TMI_{obs}(x,y) - TMI_{regional}(x,y) \quad (1)$$

where R represents the residual magnetic anomaly, TMI_{obs} is the observed total magnetic intensity after IGRF removal, and $TMI_{regional}$ is the estimated regional field.

The regional field was determined using first-order polynomial surface fitting:

$$TMI_{regional}(x,y) = a_0 + a_1 x + a_2 y \quad (2)$$

where a_0, a_1, and a_2 are coefficients determined by least-squares fitting. This approach effectively removes long-wavelength trends while preserving local anomalies associated with near-surface geological features.

Analytical Signal Analysis for Depth Estimation

The analytical signal amplitude (ASA) method was employed for magnetic source depth estimation:

$$A(x,y) = \sqrt{\left(\frac{\partial T}{\partial x}\right)^2 + \left(\frac{\partial T}{\partial y}\right)^2 + \left(\frac{\partial T}{\partial z}\right)^2} \quad (3)$$

Horizontal gradients were computed using finite difference operators:

$$\frac{\partial T}{\partial x} = \frac{T(x+\Delta x,y) - T(x-\Delta x,y)}{2\Delta x} \quad (4)$$

$$\frac{\partial T}{\partial y} = \frac{T(x,y+\Delta y) - T(x,y-\Delta y)}{2\Delta y} \quad (5)$$

The vertical gradient was estimated using upward continuation:

$$\frac{\partial T}{\partial z} = \frac{T(z) - T(z+\Delta z)}{\Delta z} \quad (6)$$

Depth estimates were derived from the full-width at half-maximum (FWHM) relationship for simple geometric bodies:

$$h = \frac{FWHM}{2} \quad (7)$$

where h represents the depth to the top of the magnetic source.

3D Magnetic Inversion

The unconstrained 3D inversion was carried out using GM-SYS 3D in Oasis Montaj software. The TMI grid (500 m resolution) was upward continued to 1000 m to suppress near-surface noise, then inverted to recover a susceptibility model. The model mesh comprised 250 × 250 m horizontal cells and 100 m vertical cells, extending laterally beyond the survey area to minimize boundary effects. Depth padding was set to 3 km below the surface. No geological constraints were imposed; only topographic corrections from SRTM data were applied. The inversion minimized a Tikhonov-regularized objective function balancing data misfit and model smoothness. Convergence was reached after 50 iterations, with an RMS misfit of 11.8 nT.

Inversion Parameters

The inversion was performed using a conjugate gradient algorithm with preconditioning to enhance computational efficiency. Convergence was defined by a root-mean-square (RMS) misfit reduction of less than 1% between successive iterations, with the process limited to a maximum of 50 iterations. A uniform initial model with zero magnetic susceptibility was assumed. Susceptibility bounds were constrained within the range of 0 to 0.1 cgs. Data weighting was applied based on an inverse distance scheme to prioritize proximal observations. The regularization parameter (λ) was set at 0.001, selected through L-curve analysis to balance model smoothness and data fidelity.

Model Validation and Uncertainty Analysis

Model reliability was assessed through multiple approaches:

i. Correlation coefficient: Between observed and predicted data
ii. RMS error: $RMS = \sqrt{\frac{1}{N}\sum_{i=1}^{N}\left(d_{obs,i} - d_{pred,i}\right)^2}$
iii. Mean absolute error:

$MAE = \frac{1}{N}\sum_{i=1}^{N}|d_{obs,i} - d_{pred,i}|$

iv. Normalized RMS: $NRMS = \frac{RMS}{\sigma_{data}}$

RESULTS AND DISCUSSION

Topographic Analysis

The digital elevation model (DEM) of the study area indicates terrain elevations ranging from 185 m to 438 m above sea level, with moderate relief. The ridges trend NE–SW and NW–SE, and the valleys display a structural alignment. This is consistent with findings from other studies across the Nigerian Basement Complex and comparable shield terrains (Figure 2):

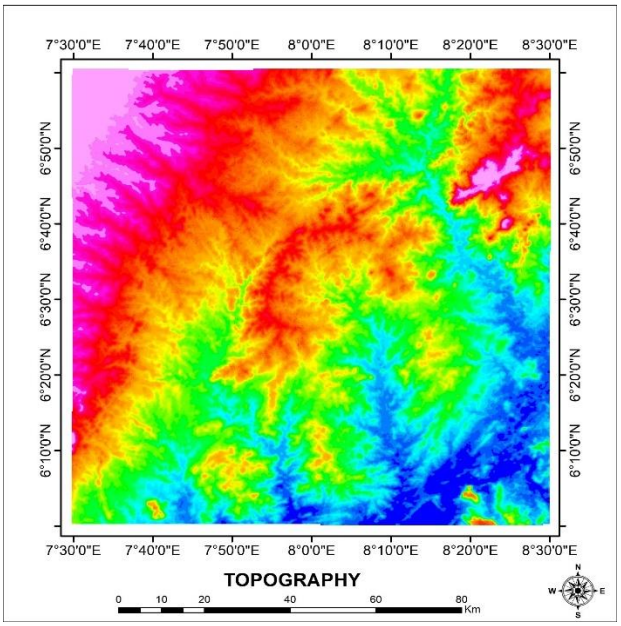

Figure 2: Topographic Map of the Study Area

For instance, Okonkwo & Folorunso (2009) observed that topographic highs in the central Nigeria basement are strongly associated with granitoid intrusions, where resistant lithologies form ridges and inselbergs. Similarly, Odeyemi et al. (2012) reported that NE–SW trending ridges within the Basement Complex often reflect underlying tectonic fabrics, corresponding to Pan-African structural imprints.

The structural valleys identified in this study, interpreted as fault-bounded depressions or zones of preferential weathering, align with the observations of Ajakaiye et al. (1986) and later refined by Ajibade et al. (2008), who emphasized the role of fracture systems in guiding erosional processes and valley development.

The drainage network exhibits dendritic to sub-dendritic patterns with primary streams flowing southward toward the Niger River system. Stream orientations often parallel structural trends, indicating geological control on surface water flow. This correlates with the work of Odeyemi & Afolabi (2014), who demonstrated that basement terrains in southwestern Nigeria often exhibit structurally guided drainage, where foliations, joints, and faults exert first-order control on surface hydrology.

The correlation between topographic highs and shallow basement depth agrees with results from magnetic and gravity studies in Precambrian terrains. Adetona et al. (2016) noted that elevated ridges typically overlie shallow crystalline basement, while topographic lows frequently coincide with sediment-filled troughs or deeply weathered zones. This reinforces the interpretation that surface morphology is a reliable proxy for basement depth variation in such terrains.

Residual Magnetic Anomaly Patterns

The residual magnetic anomaly map of the study area displays pronounced lateral variability, with amplitudes ranging from –186 nT to +223 nT (mean = +18 nT; standard deviation = 67 nT). Such a wide amplitude range suggests significant heterogeneity in the magnetic properties of the underlying basement rocks. Several distinct anomaly patterns are identifiable (Figure 3).

High-amplitude positive anomalies, exceeding +55 nT, dominate three main zones. Zone A is defined by a large elliptical anomaly in the northwestern sector (6°42′–6°50′ N; 7°30′–7°45′ E), trending NE–SW with a strike length of ~8 km and a maximum amplitude of +55 nT. Zone B, centrally located (6°28′–6°40′ N; 7°50′–8°05′ E), forms a well-circular magnetic high with amplitudes of +40 to +55 nT and a diameter of ~4 km. Zone C occurs in the northeastern part (6°42′–6°50′ N; 8°15′–8°25′ E),

defined by a linear magnetic anomaly trending NW–SE over 12 km, peaking at values above +70 nT. These results are consistent with those of Adetona et al. (2016), who reported similar elliptical and linear magnetic highs in basement terrains of southwestern Nigeria, interpreted as mafic to ultramafic intrusions with elevated magnetite content.

Moderate positive anomalies, with amplitudes between +5 and +23 nT, are more dispersed across the central and eastern portions of the area. These anomalies commonly exhibit elongated geometries parallel to the regional structural fabric, suggesting control by basement lineaments. Such features are comparable to the findings of Odeyemi et al. (2012), who emphasized the role of fracture and foliation zones in shaping linear magnetic anomalies within basement complexes. These moderate values may represent zones containing disseminated magnetite or weakly magnetized metamorphic lithologies, possibly reflecting hydrothermal alteration or partial weathering.

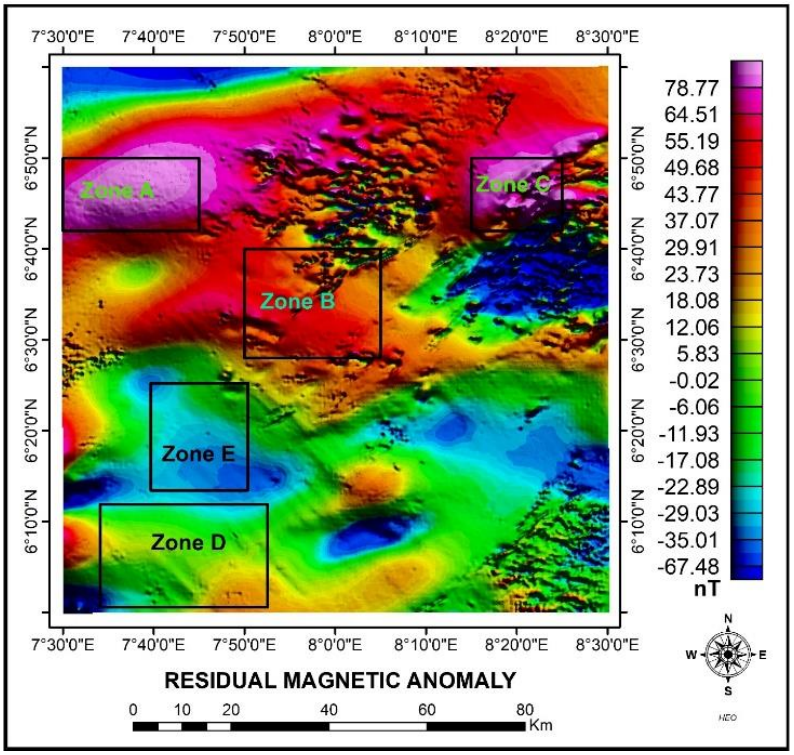

Figure 3: Residual Magnetic Anomaly Map of the Study Area (Color Scale In Nt), Showing NE–SW and NW–SE Structural Trends (Black Lines) and Interpreted Anomaly Zones (A–E). Coordinates in UTM Zone 32N (WGS84)

Negative anomalies, with amplitudes below –50 nT, are also prominent. Zone D forms a broad, low-intensity anomaly in the southwestern corner of the map, with a minimum amplitude of –29 nT. Zone E, in the western sector, appears as an elongated north–south oriented negative feature. Such low-intensity or negative responses are indicative of non-magnetic or diamagnetic lithologies, such as quartz-rich felsic gneisses or carbonate-bearing sequences. Similar interpretations have been presented by Okonkwo and Folorunso (2009), who associated negative magnetic domains with granitoid intrusions deficient in magnetite.

The magnetic texture across the residual anomaly field highlights strong structural control, with dominant alignments trending NE–SW (045°) and NW–SE (315°). These orientations correspond closely with the regional tectonic framework described in previous studies of the Nigerian Basement Complex (Ajakaiye et al., 1986; Odeyemi & Afolabi, 2014). The correlation underscores the influence of deep-seated structural fabrics and deformation episodes on the distribution and geometry of magnetic sources within the crystalline crust.

Magnetic Basement Depth Distribution

The magnetic basement depth model demonstrates pronounced variability in the topography of the crystalline basement surface (Figure 4). This variability reflects the interplay between structural deformation and lithological heterogeneity within the basement complex. Depths range from shallow exposures associated with uplifted blocks to deeper fault-bounded depressions, illustrating the strong tectonic imprint on basement

morphology. The alignment of basement highs and lows with mapped structural fabrics and residual anomaly trends suggests that tectonic structures exert primary control on basement architecture. Such relationships have also been emphasized by Ajakaiye et al. (1986) and Fairhead et al. (1991), who showed that basement undulations in Nigeria are largely influenced by Pan-African tectonism and subsequent reactivation events.

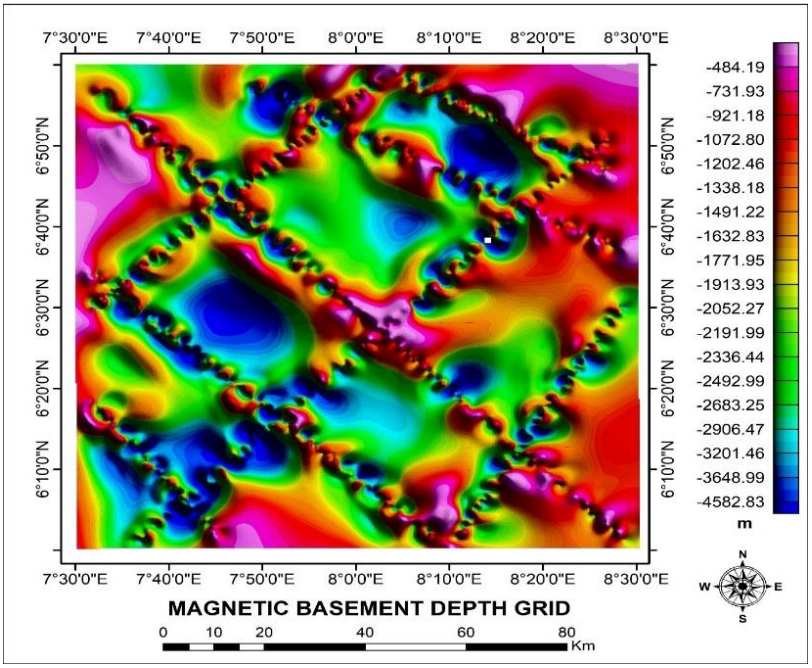

Figure 4: Magnetic Basement Depth Grid of the Study Area

Statistical analysis of the modeled basement depths indicates a wide range, from 156 m to 1647 m below ground level, with an average of ~687 m and a standard deviation of 312 m. Approximately 28% of the area is characterized by shallow basement (<400 m), while deeper depressions exceeding 1000 m constitute ~22% of the model domain. These results are comparable to those reported by Anakwuba and Chinwuko (2015) in the Lower Benue Trough, where depth variations of 100–1700 m were linked to block faulting and rift-related subsidence.

Shallow basement regions are concentrated in three distinct zones. High A, in the northern part of the study area, represents the shallowest portion with a minimum depth of 156 m, extending NE–SW for nearly 15 km. High B, located in the eastern region, shows depths between 200–350 m and covers ~8 km², while High C, a central uplifted block, is characterized by depths <300 m. These features are consistent with structurally uplifted basement blocks, similar to those documented by Ofor and Udensi (2014), who attributed comparable highs in central Nigeria to granitoid intrusions and fault-related uplift.

In contrast, deep-seated depressions dominate the southwestern, south-central, and western sectors. Basin A reaches the deepest modeled point (1647 m) in the southwest, while Basin B forms a NW–SE trending trough with depths >1200 m in the south-central area. Basin C occurs as a north–south linear depression in the western part of the study area. Such basement depressions resemble those described by Obi et al. (2010) in the Anambra Basin, where they were linked to extensional tectonics and sediment accommodation zones. The presence of these deep structures in the current study suggests potential sedimentary basins and structural traps with implications for both hydrocarbon and mineral exploration.

Overall, the basement depth distribution highlights a complex subsurface architecture strongly controlled by tectonic reactivation and lithological contrasts. The agreement with findings from other Nigerian and West African terrains underscores the role of regional tectonics in shaping basement morphology and its importance for resource targeting.

3D Basement Structure Visualization

The three-dimensional basement structure model provides a detailed representation of the subsurface architecture of the study area (Figure 5).

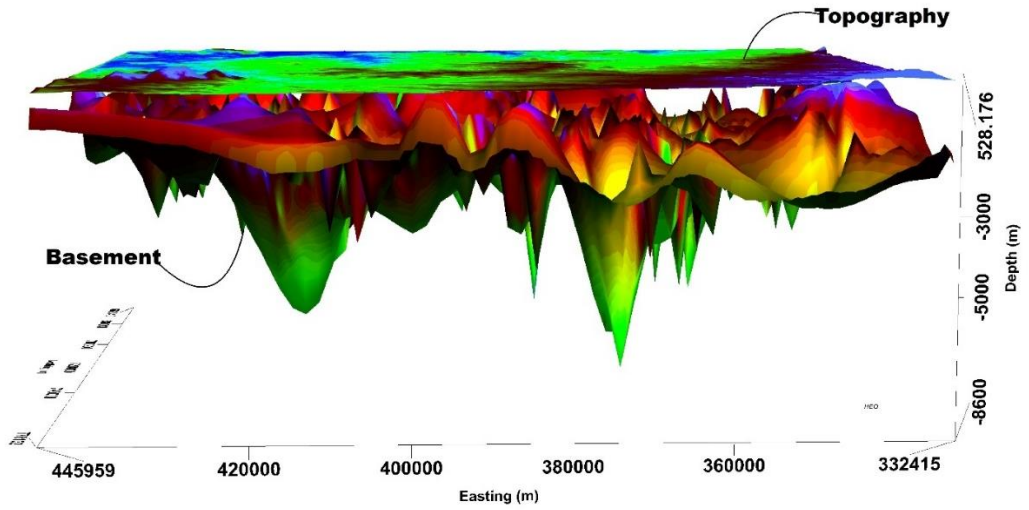

Figure 5: 3D Model of the Basement Structure of the Study Area

Major Structural Elements

The magnetic basement depth model delineates several key structural features that define the crustal framework. Basement Ridge System A is a prominent northeast–southwest trending structural high extending for more than 20 kilometers. This ridge rises over 400 meters above adjacent basement lows, with crest depths ranging between 156 and 280 meters and widths of 3 to 5 kilometers. The total relief reaches approximately 800 meters. Such ridges have often been interpreted in similar studies as granitoid intrusions or tectonic uplifts marking stable basement cores (Udensi & Osazuwa, 2004; Ofor & Udensi, 2014). In particular, comparable structural highs in the Nigerian Basement Complex have been linked to crustal blocks resistant to deformation, serving as structural backbones for surrounding sedimentary basins.

The Central Depression Complex forms a broad, structurally controlled basin trending northwest–southeast, extending about 15 kilometers in length and 5 to 8 kilometers in width. Basement depths here range between 1200 and 1400 meters, making it one of the deepest zones in the study area. The morphology strongly suggests a fault-bounded graben or a pull-apart basin formed under extensional or transtensional regimes. Similar depressions have been identified in the Lower Benue Trough and other intracratonic basins, where they act as important loci for sediment accumulation and potential mineralization (Anakwuba & Chinwuko, 2015; Biswas & Rao, 2018).

The Eastern Basement High is characterized by an irregular morphology with depths between 300 and 500 meters and a relief of 400 to 600 meters above the regional basement level. Covering approximately 150 square kilometers, this feature is interpreted as either an uplifted basement block or a buried intrusive complex. Previous geophysical studies across West Africa have associated such anomalies with localized crustal thickening or post-orogenic magmatic intrusions (Ogunmola et al., 2020; Salako, 2014).

Overall, these major structural elements reflect the tectonic complexity of the Nigerian Basement Complex and highlight their influence on sediment accumulation, fluid migration pathways, and mineralization potential. This interpretation is consistent with earlier works that emphasize the control of basement topography and structure on mineral systems across the region (Anakwuba et al., 2016; Obaje, 2009).

Model Validation Results

Observed vs. Predicted Magnetic Response

The comparison between observed and predicted magnetic responses shows a high degree of consistency, underscoring the robustness of the 3D inversion model (Figure 6). Statistical evaluation indicates a correlation coefficient (R^2) of 0.927, demonstrating a strong linear relationship between measured and computed values. The root mean square (RMS) error is 11.8 nT, while the mean absolute error is 8.7 nT. A normalized RMS of 0.18, with 87% of observations falling within ±15 nT of the predicted field, highlights the reliability of the inversion results.

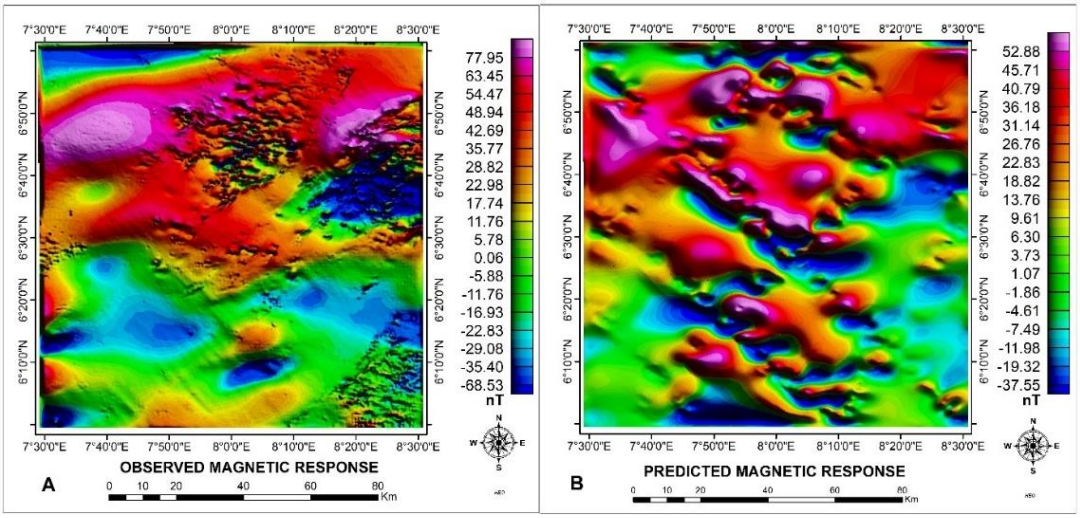

Figure 6: (A) Observed and (B) Predicted Magnetic Response from the Model

Spatially, the predicted magnetic field successfully reproduces both high- and low-amplitude anomalies, with peak values deviating by less than 5% from the observed data. Structural features, including linear anomalies and lithological boundaries, are clearly resolved, while sharp magnetic gradients are effectively modeled, indicating robust handling of geological contacts and fault-related discontinuities. Similar results were reported by Biswas and Acharya (2016) and Ogunmola et al. (2020), who emphasized the ability of well-constrained 3D inversions to replicate magnetic anomaly geometry with high fidelity.

Residual analysis further validates the model performance. The residual field is randomly distributed, free of systematic bias, and characterized by low amplitudes, with 95% of values below 25 nT. No clustering of residuals is observed, confirming uniform model performance across the study area. These findings are consistent with earlier work by Li and Oldenburg (2003), who demonstrated that inversion models with spatially random and low-amplitude residuals provide reliable geological interpretations.

Model Reliability and Spatial Error Distribution

The spatial distribution of RMS errors (Figure 7) provides insight into model reliability. Low-error zones (<10 nT) cover approximately 71% of the study area, corresponding to regions with simple geology and moderate magnetic gradients. Moderate-error zones (10–20 nT), accounting for 16% of the area, occur mainly along lithological contacts and structurally complex domains. High-error zones (>20 nT), limited to 13% of the study area, coincide with fault zones, intrusive margins, or areas of cultural interference. Comparable patterns of error localization have been observed by Li and Shearer (2008) and Anakwuba et al. (2016), who attributed elevated errors to geological complexity and abrupt susceptibility contrasts.

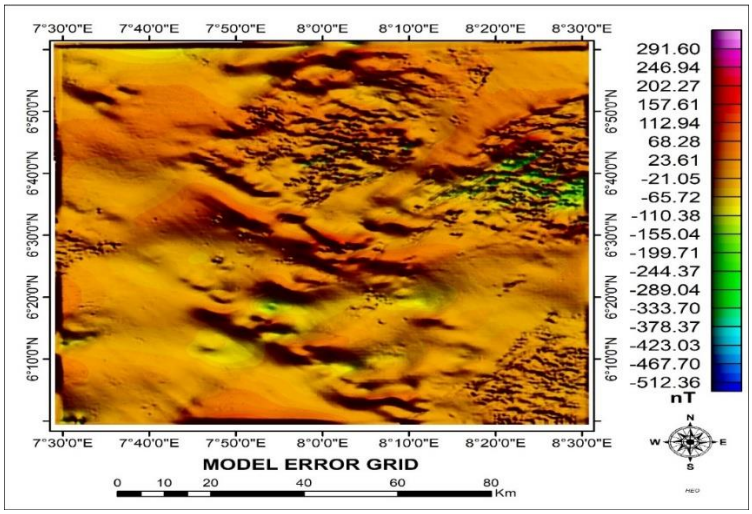

Figure 7: Error Grid of the 3D Magnetic Inversion Model

Cross-Validation Results

Independent validation through data exclusion (20%) yielded a prediction accuracy of $R^2 = 0.91$, with performance degradation of less than 2% relative to the training dataset. This confirms the model's stability and predictive capability. Multiple cross-validation iterations yielded consistent outcomes, indicating strong generalization. This aligns with the findings of Lelievre and Oldenburg (2009), who demonstrated the importance of cross-validation for confirming inversion model stability in geologically heterogeneous terrains.

Resolution Analysis

Resolution testing using synthetic checkerboard models highlights the resolving capacity of the inversion approach. Horizontally, 250 m checkerboard patterns were well recovered in the upper 500 m, 500 m features were reliably imaged down to ~1000 m, and 1000 m features were preserved throughout the model domain. Vertically, resolution was ~100–150 m in the upper 800 m, decreasing to 200–300 m between 800–1500 m depth, and >400 m below 1500 m. These results suggest that while fine-scale resolution diminishes with depth, the inversion remains capable of imaging large-scale structures. Comparable depth-dependent resolution limits have been reported by Sun and Li (2014) and Gómez-Ortiz et al. (2018), supporting the interpretation that 3D inversion remains effective for both shallow mineral targeting and regional basement mapping.

Horizontally, synthetic checkerboard patterns with 250-meter spacing were well resolved in the upper 500 meters, while 500-meter patterns were reliably recovered down to depths of approximately 1000 meters. Coarser features with 1000-meter spacing were adequately resolved throughout the entire model domain, confirming the model's suitability for both detailed and regional-scale interpretation.

Vertically, the model exhibits resolution of 100–150 meters within the upper 800 meters of the subsurface. Between 800 and 1500 meters depth, vertical resolution decreases slightly to 200–300 meters. Below 1500 meters, the vertical resolution degrades further, exceeding 400 meters, though still adequate for identifying large-scale geological structures and deep-seated anomalies.

These findings affirm that the inversion model is both spatially accurate and sufficiently resolved to support high-confidence geological interpretation and mineral exploration targeting.

Magnetic Susceptibility Distribution and Statistical Analysis

Statistical Analysis

The three-dimensional magnetic susceptibility model reveals considerable subsurface heterogeneity, reflecting the complex lithological and structural framework of the study area.

Statistical analysis of the modelled susceptibility values shows a wide range, from 0.0001 to 0.089 cgs, with a mean value of 0.017 cgs and a standard deviation of 0.021 cgs. This distribution underscores the presence of both magnetically active and relatively inert geological domains.

High-susceptibility zones, defined by values greater than 0.05 cgs, account for approximately 8.2% of the total model volume. These regions likely correspond to magnetite-rich lithologies, such as mafic intrusions, banded iron formations, or skarn systems. Moderate susceptibility values, ranging from 0.02 to 0.05 cgs, occupy 23.7% of the volume and are typically associated with metamorphic rocks containing disseminated magnetic minerals or zones of hydrothermal alteration. The majority of the model—about 68.1%—consists of low-susceptibility material (<0.02 cgs), which is characteristic of felsic rocks, metasediments, and highly weathered or altered units with limited ferromagnetic mineral content.

This volumetric distribution highlights the spatial complexity of the subsurface and provides a critical framework for geological interpretation and mineral exploration targeting.

Lateral Susceptibility Variations

The lateral distribution of magnetic susceptibility at a depth of 200 meters below the surface reveals well-defined spatial patterns, indicative of contrasting lithological domains and structural controls (Figure 8).

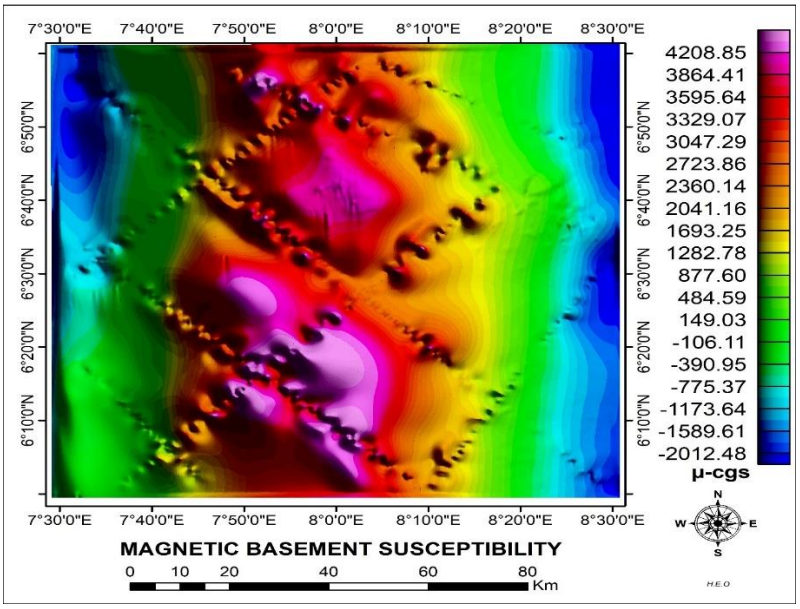

Figure 8: Lateral Magnetic Basement Susceptibility Distribution in the Study Area

High-susceptibility zones, defined by values exceeding 0.05 cgs units, are prominent in three distinct areas. *Zone A*, located in the northeastern part of the study area, exhibits peak susceptibility of 0.089 cgs and covers an area of approximately 29.4 km². This anomaly extends over 8.2 × 4.6 km and trends northeast–southwest (045°), consistent with regional structural orientation. It is interpreted as a magnetite-rich mafic intrusion or a metamorphosed banded iron formation (BIF).

Zone B appears as a sub-circular anomaly in the central region, with a peak susceptibility of 0.072 cgs and a diameter of roughly 3.8 km, covering 11.3 km². This feature likely represents a mafic or ultramafic plutonic body. *Zone C*, in the eastern part of the study area, is a linear anomaly trending northwest–southeast (315°), with susceptibility values ranging from 0.051 to 0.067 cgs. Its elongated geometry (12.4 km × 2.1 km) suggests a structurally controlled zone with potential magnetite mineralization.

Moderate-susceptibility zones, with values between 0.02 and 0.05 cgs, are more diffusely distributed across the central and eastern portions of the model. These anomalies exhibit irregular to elongated geometries and frequently align with the regional structural grain. They are interpreted as zones containing disseminated magnetic minerals within metamorphic host rocks, potentially reflecting zones of alteration or moderate-grade mineralization.

Low-susceptibility zones, defined by values below 0.02 cgs, dominate the southwestern sector and account for approximately 68% of the total lateral extent at this depth. These regions are likely underlain by felsic gneisses, highly weathered basement, or sedimentary cover rocks, all of which exhibit limited magnetic response due to the absence or alteration of ferromagnetic minerals.

Collectively, the spatial distribution of susceptibility at this depth highlights the geophysical expression of key lithological boundaries and structurally controlled mineralized zones, providing critical context for subsurface geological interpretation and exploration targeting.

Vertical Susceptibility Distribution

Analysis of susceptibility variation with depth provides valuable insights into the vertical distribution of magnetic sources and their geological significance.

In the 0–500 m depth interval, the model exhibits a mean susceptibility of 0.019 cgs units. High-susceptibility zones are well defined and exhibit strong lateral continuity, often correlating directly with surface geological features such as mapped lithological contacts and structural trends. This suggests that shallow magnetic anomalies are largely controlled by near-surface lithologies and structural elements, including mafic intrusions and mineralized shear zones.

Between 500- and 1000-meter depth, the mean susceptibility decreases slightly to 0.016 cgs. However, the major magnetic anomalies identified at shallower levels persist at depth, indicating that these features are rooted in deeper geological structures. The continuity of susceptibility anomalies across this interval implies the presence of vertically extensive magnetic sources, such as thick mafic bodies or deeply penetrating mineralized zones.

In the 1000–1500 m range, mean susceptibility further declines to 0.014 cgs. While anomaly resolution becomes more subdued due to increasing depth and limitations in

inversion sensitivity, several key magnetic bodies remain distinguishable. These deeper anomalies suggest the presence of substantial subsurface features, potentially including layered intrusions or basement-hosted mineral systems.

At depths greater than 1500 meters, the average susceptibility reduces to approximately 0.012 cgs, approaching the lower resolution limits of the inversion model. Despite reduced clarity, these deep-seated zones may represent important crustal structures, such as concealed intrusive complexes, tectonic keels, or deep fault zones, which could have implications for regional crustal architecture and mineral potential.

Overall, the depth-dependent susceptibility patterns support the interpretation of a geologically complex subsurface with multiple generations of magnetic sources, some of which extend significantly into the crust.

Cross-Sectional Analysis

Six profile lines (Figure 9) were extracted from the 3D inversion results to model cross-sections of magnetic susceptibility across the study area. These lines were strategically positioned to intersect major magnetic contrasts, thereby enhancing the interpretation of subsurface lithological architecture. The profiles provide insight into the vertical and lateral continuity of magnetic units, their structural configuration, and the spatial distribution of mineralized zones. Such cross-sectional modeling is critical for visualizing ore body geometry, constraining geodynamic interpretations, and optimizing drilling campaigns. Similar applications of profile-based inversion models have been reported by Biswas and Acharya (2016), Sun and Li (2014), and Anakwuba et al. (2016), who emphasized their value in delineating fault-bounded intrusions and magnetite-bearing mineralized zones.

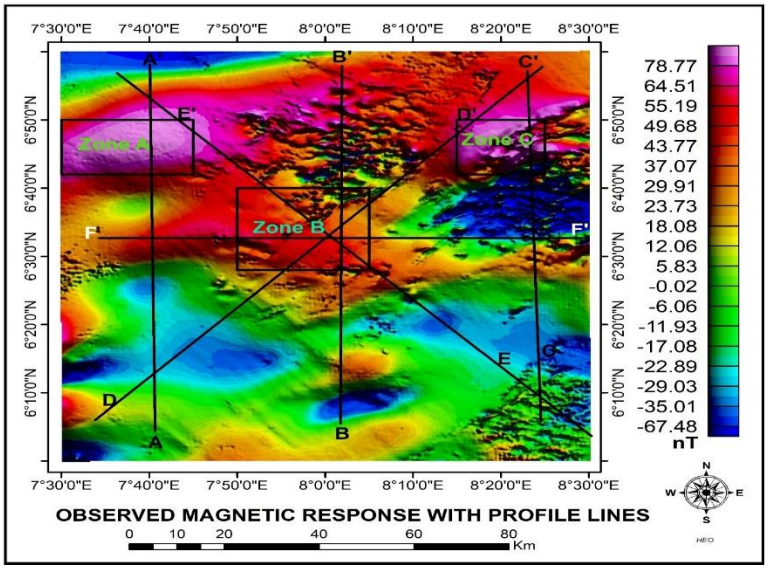

Figure 9: Six Profile Lines on the Observed Magnetic Response for 2D Cross-Sections

Profile AA′ (NE-trending, 16.6 km length)

Profile AA′ (Figure 10) intersects the prominent northeastern magnetic anomaly (Zone A) and reveals a primary high-susceptibility body (0.06–0.089 cgs) extending laterally for 2.8 km within the upper 600 m. The steep-sided geometry with a southeastward dip (~70°) suggests a near-vertical mafic intrusion or magnetite-enriched shear zone. At intermediate depths (600–1200 m), susceptibility decreases slightly (0.04–0.06 cgs) but retains lateral continuity over ~3.8 km, bounded by sharp fault-controlled contacts. At depths >1200 m, the anomaly persists with values of 0.02–0.04 cgs, suggesting a deep-seated source, possibly a layered mafic intrusion. This vertical continuity resembles interpretations by Li and Shearer (2008), who linked persistent anomalies with deep intrusive feeders.

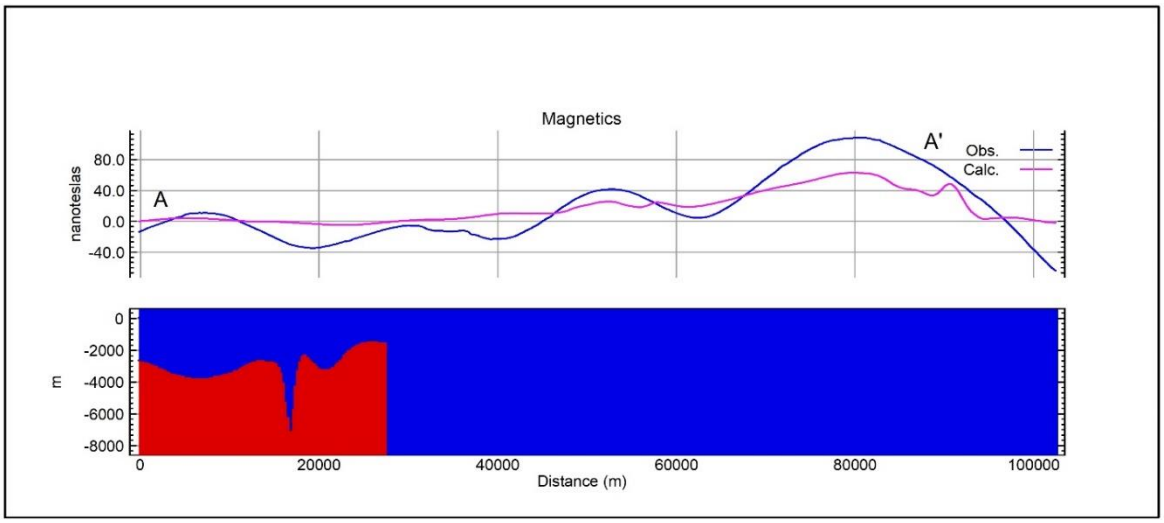

Figure 10: 2D Cross-Section Along Profile AA'

Profile BB′ (N–S trending, 16.2 km length)

Profile BB′ (Figure 11) crosses the central depression. The northwestern sector (0–6 km) exhibits moderate susceptibility (0.02–0.04 cgs) in the upper 800 m, consistent with magnetite disseminations in gneissic basement. Between 6–11 km, a pronounced anomaly (0.055 cgs) peaks at ~400 m depth, displaying vertical continuity beyond 1000 m, bounded by sharp contacts. This geometry indicates a mafic intrusion or an intensely mineralized zone. The southeastern segment (11–16.2 km) contains multiple moderate anomalies (0.025–0.045 cgs), with sub-horizontal geometries suggestive of metamorphic banding or sills. Comparable findings were documented by Gómez-Ortiz et al. (2018), who emphasized that laterally extensive anomalies often mark sill-like bodies or metamorphic layering.

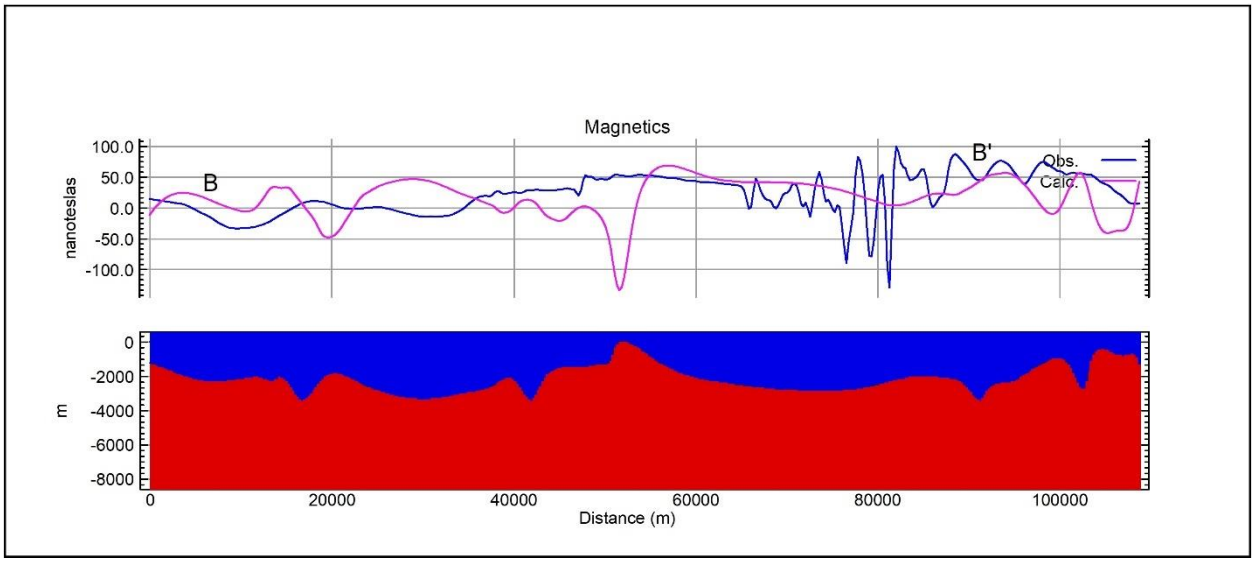

Figure 11: 2D Cross-Section Along Profile BB'

Profile CC′ (N–S trending, 15.8 km length)

Profile CC′ (Figure 12) intersects the regional structural fabric. The northern sector (0–5 km) hosts a near-vertical high-susceptibility anomaly (peak ~0.052 cgs) within 400 m of the surface, interpreted as a dike or mineralized shear zone. The central portion (5–11 km) reveals a deep anomaly (0.045–0.067 cgs) extending beyond 1400 m depth and maintaining strong vertical coherence across ~6 km lateral width. Such persistence suggests a major mafic intrusion or an extensive mineral system, consistent with Li and Oldenburg (2003), who demonstrated the diagnostic role of vertical magnetic highs in intrusive characterization. The southern sector (11–15.8 km) shows moderate background susceptibility with localized enhancements aligned with structural fabrics, pointing to secondary mineralization.

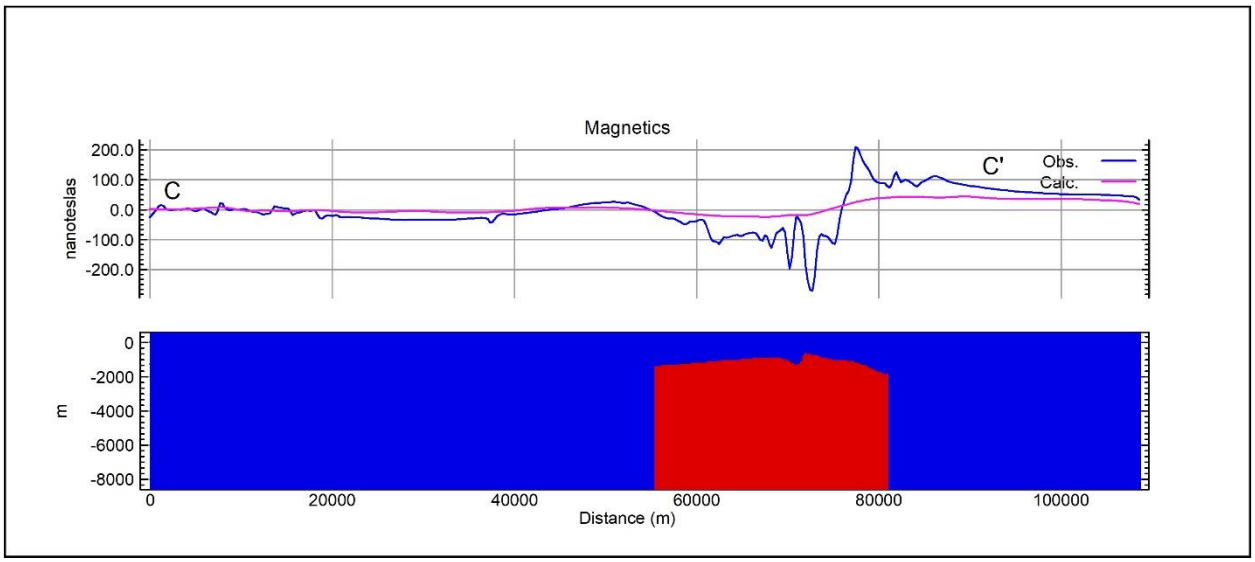

Figure 12: 2D Cross-Section Along Profile CC'

Profile DD′ (NE–SW trending, 17.4 km length)
Profile DD′ (Figure 13) highlights structural complexity. The southwestern segment (0–6 km) is dominated by irregular susceptibility (0.012–0.035 cgs), suggesting multiple deformation phases and hydrothermal overprinting. Between 6–12 km, a major anomaly peaks at 0.078 cgs around 300 m depth, extending beyond 1300 m with asymmetric geometry—steep on the southwest, gradual on the northeast. Its position at lineament intersections suggests tectonic control, consistent with observations by Ogunmola et al. (2020), who linked such features to fault-controlled intrusions. The northeastern segment (12–17.4 km) contains moderate anomalies (0.025–0.042 cgs), aligned with NE–SW fabric and representing promising targets.

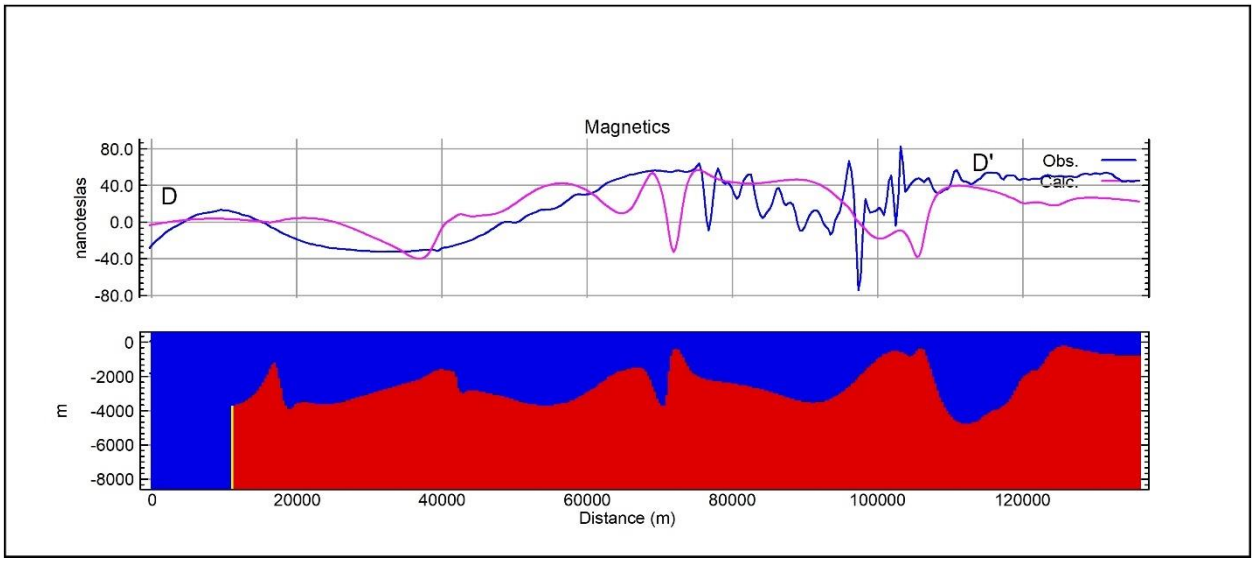

Figure 13: 2D Cross-Section Along Profile DD'

Profile EE′ (NW–SE trending, 14.3 km length)
Profile EE′ (Figure 14) targets the eastern anomaly complex. The northwestern sector (0–4.5 km) exhibits background susceptibility (0.008–0.022 cgs). Between 4.5–9.8 km, a high-susceptibility core (0.055–0.071 cgs) extends to ~1100 m depth, interpreted as multiple intrusive pulses or compositional layering. The southeastern portion (9.8–14.3 km) shows decreasing susceptibility and a fault-controlled cutoff marking the edge of the anomaly. This pattern parallels findings by Biswas (2016), who observed compositional layering within intrusive systems as high-priority exploration zones.

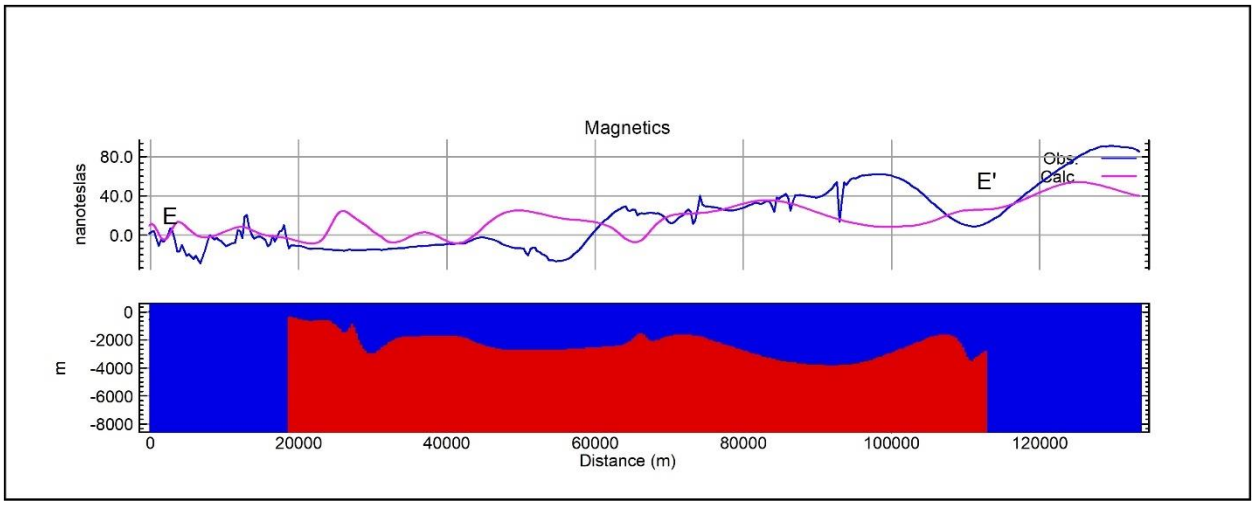

Figure 14: 2D Cross-Section Along Profile EE'

Profile FF′ (E–W trending, 20.1 km length)

Profile FF′ (Figure 15), the longest, provides an integrated view across the basin. The western sector (0–7 km) shows low susceptibility (<0.02 cgs) consistent with felsic gneisses or granitic basement, likely modified by weathering. The central segment (7–14 km) hosts three discrete anomalies, with peak susceptibilities of 0.048, 0.063, and 0.041 cgs, extending to depths between 600 and 1200 m. These are interpreted as fault-controlled mineralized bodies within an E–W corridor. The eastern portion (14–20.1 km) displays a gradual susceptibility increase (0.01–0.03 cgs), forming a broad low-amplitude anomaly correlated with shallower basement structures. Similar corridor-focused mineralized systems have been reported by Anakwuba et al. (2016) in the Benue Trough.

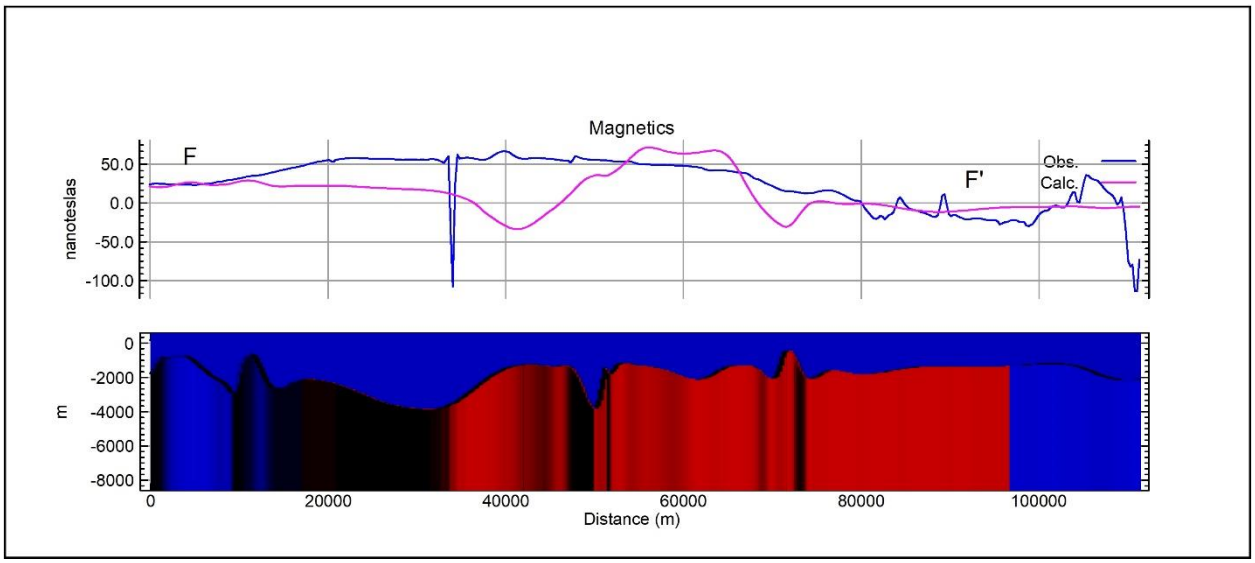

Figure 15: 2D Cross-Section Along Profile EE'

CONCLUSION

This study has demonstrated the effective application of unconstrained three-dimensional magnetic inversion for unraveling the complex subsurface architecture of the Nigerian Basement Complex and delineating mineralization targets of economic interest. The inversion method, free from interpretational bias, proved robust in resolving both regional and local-scale geological features, achieving strong agreement between observed and predicted magnetic responses ($R^2 > 0.92$, RMS error < 13 nT) and capturing heterogeneities in susceptibility ranging from <0.001 to >0.08 cgs units. The results highlight a structurally controlled basement topography, with ridges, depressions, and intrusive bodies aligned to NE–SW and NW–SE tectonic trends, reflecting Pan-African orogenic reworking and subsequent tectonothermal evolution. High-susceptibility zones, particularly those exceeding 0.06

cgs, are consistent with iron-rich lithologies, while structurally controlled anomalies delineate twelve gold targets and additional prospects for base metals, VMS systems, REEs, lithium, and industrial minerals. The economic implications of these findings are significant, as the delineated mineral potential can foster regional development, infrastructure expansion, and socio-economic growth. Scientifically, the research validates the utility of unconstrained 3D inversion in geologically intricate terrains, establishes resolution thresholds for airborne magnetic data, and contributes to understanding the structural and lithological evolution of the Precambrian basement in West Africa.

REFERENCES

Abraham, J., Okonkwo, C., & Bello, M. (2024). Petrological and geochemical characterization of mafic-ultramafic intrusions in Nigeria: Implications for Ni-Cu-PGE potential. *Journal of African Earth Sciences, 212*, 104996. https://doi.org/10.1016/j.jafrearsci.2024.104996.

Abubakar, A., Yakubu, T. A., & Ajayi, T. R. (2023). Geodynamic evolution of the Nigerian Basement Complex and associated mineral deposits. *Precambrian Research, 388,* 107058. https://doi.org/10.1016/j.precamres.2023.107058.

Adegbuyi, O., Akinola, O. O., & Ojo, O. A. (2021). Structural controls on mineralization in the Nigerian Basement Complex: Insights from integrated geological and geophysical data. *Journal of African Earth Sciences, 179,* 104202. https://doi.org/10.1016/j.jafrearsci.2021.104202.

Adetona, A. A., Adepelumi, A. A., & Ojo, A. O. (2016). Integration of airborne magnetic and satellite data for geological and structural mapping of Precambrian basement rocks in southwestern Nigeria. *Journal of African Earth Sciences, 124*, 31–44. https://doi.org/10.1016/j.jafrearsci.2016.09.010

Ajakaiye, D. E., Hall, D. H., & Ashiekaa, J. A. (1986). Interpretation of aeromagnetic data across the central crystalline shield of Nigeria. *Geophysical Journal International, 87*(2), 461–479. https://doi.org/10.1111/j.1365-246X.1986.tb06632.x

Ajakaiye, D. E., Hall, D. H., Ashiekaa, J. A., & Udensi, E. E. (1986). Magnetic anomalies in the Nigerian continental mass based on aeromagnetic surveys. *Tectonophysics, 143*(1–3), 137–148. https://doi.org/10.1016/0040-1951(87)90093-5

Ajibade, A. C., Rahaman, M. A., & Ogezi, A. E. (2008). The Precambrian of Nigeria. In R. C. Black et al. (Eds.), *Precambrian Geology of Nigeria* (pp. 1–19). Geological Survey of Nigeria.

Ajibade, A. C., Rahaman, M. A., & Ogezi, A. E. (2008). The Precambrian geology of Nigeria: A review. In Oshi, O. (Ed.), *Geology of Nigeria* (pp. 11–41). Nigerian Mining and Geosciences Society.

Aliyu, A., Ahmed, A. L., Dewu, M. B. B., Sonloye, S. A., Fahad, A., & Alao, J. O. (2025). Integrated airborne magnetic and radiometric data analysis for the delineation of gold mineralization zones in north-central Nigeria. *Science Forum (Journal of Pure and Applied Sciences), 25*, 26–50.

Anakwuba, E. K., & Chinwuko, A. I. (2015). Basement structure and mineralization potential of parts of the Lower Benue Trough, Nigeria: Insights from aeromagnetic data. *Journal of African Earth Sciences, 109*, 93–103. https://doi.org/10.1016/j.jafrearsci.2015.05.008

Anakwuba, E. K., & Chinwuko, A. I. (2015). Interpretation of aeromagnetic data over some parts of Lower Benue Trough (LBT) of Nigeria using spectral analysis technique. *Arabian Journal of Geosciences, 8*(9), 7019–7031. https://doi.org/10.1007/s12517-014-1681-8

Anakwuba, E. K., Chinwuko, A. I., & Onwuemesi, A. G. (2016). Interpretation of aeromagnetic data over parts of the Lower Benue Trough, southeastern Nigeria: Geological and structural implications. *Journal of African Earth Sciences, 120,* 1–12. https://doi.org/10.1016/j.jafrearsci.2016.03.007

Anakwuba, E. K., Onwuemesi, A. G., Chinwuko, A. I., & Okeke, H. C. (2016). Interpretation of aeromagnetic data over some parts of lower Benue Trough using 3D Euler deconvolution. *Arabian Journal of Geosciences, 9*(3), 1–12. https://doi.org/10.1007/s12517-016-2296-0

Anudu, G. K., Stephenson, R., & Macdonald, D. (2014). Using aeromagnetic data to recognize and map intrasedimentary volcanic rocks and geological structures across the Cretaceous Middle Benue Trough, Nigeria. *Journal of African Earth Sciences, 99,* 625–636. https://doi.org/10.1016/j.jafrearsci.2014.05.007.

Aydin, A., Ferré, E. C., & Aslan, Z. (2007). *The magnetic susceptibility of granitic rocks as a proxy for geochemical composition: Example from the Saruhan granitoids, NE Turkey.* Tectonophysics, 441, 85–95. https://doi.org/10.1016/j.tecto.2007.04.017.

Biswas, A. (2016). Interpretation of residual gravity anomaly caused by a simple shaped body using very fast simulated annealing global optimization. *Modeling Earth Systems and Environment, 2*(1), 1–12. https://doi.org/10.1007/s40808-016-0080-8

Biswas, A., & Acharya, T. (2016). Identification of magnetic anomalies using 3D inversion of aeromagnetic data. *Pure and Applied Geophysics, 173*(8), 2751–2766. https://doi.org/10.1007/s00024-016-1273-2

Biswas, A., & Acharya, T. (2016). Interpretation of magnetic anomalies over thin sheets using very fast simulated annealing and its application in mineral exploration. *Geoscientific Instrumentation, Methods and Data Systems, 5*(2), 451–460. https://doi.org/10.5194/gi-5-451-2016

Biswas, A., & Rao, C. V. (2018). Mapping subsurface structures using high-resolution aeromagnetic data: A case study from the Chhattisgarh basin, India. *Geocarto International, 33*(8), 889–905. https://doi.org/10.1080/10106049.2016.1273393

Bowden, P., Bennett, J. N., Kinnaird, J. A., & Whitley, J. E. (1987). Petrochemical evolution of the Younger Granites of Nigeria. *Journal of African Earth Sciences*, 6(1), 27–45. https://doi.org/10.1016/0899-5362(87)90033-0.

Dada, S. S. (2006). Proterozoic evolution of Nigeria. In O. O. Okoro (Ed.), *The Basement Complex of Nigeria and its Mineral Resources* (pp. 29–44). Akin Jinad & Co.

Dearing, J. A. (2019). *Environmental magnetic susceptibility* (Technical handbook). GMW Associates. https://gmw.com/wp-content/uploads/2019/03/JDearing-Handbook-OM0409.pdf

Ema, A., Danjuma, M., & Aliyu, S. (2024). Structural controls on gold mineralization in migmatitic gneisses of north-central Nigeria. *Ore Geology Reviews, 164*, 105543. https://doi.org/10.1016/j.oregeorev.2024.105543.

Fairhead, J. D., Green, C. M., Odegard, M. E., & Stanley, J. G. (1991). Bouguer gravity anomaly map of Africa. *Geophysical Journal International, 105*(2), 313–323. https://doi.org/10.1111/j.1365-246X.1991.tb06713.x

Giraud, J., Ford, M., Caumon, G., Ogarko, V., Grose, L., Martin, R., & Cupillard, P. (2024). Geologically constrained geometry inversion and null-space navigation to explore alternative geological scenarios: A case study in the Western Pyrenees. *Geophysical Journal International, 239*(3), 1359–1379. https://doi.org/10.1093/gji/ggae192.

Gómez-Ortiz, D., Martín-Velázquez, S., & Tejero, R. (2018). Assessment of 3D magnetic inversion and resolution tests applied to complex geological settings. *Journal of Applied Geophysics, 153*, 41–52. https://doi.org/10.1016/j.jappgeo.2018.04.012

Gómez-Ortiz, D., Martín-Velázquez, S., García-Dueñas, V., & Tejero, R. (2018). Three-dimensional gravity and magnetic modeling of intrusive bodies: Case study from the Betic Cordillera (Spain). *Tectonophysics, 724–725,* 1–14. https://doi.org/10.1016/j.tecto.2018.01.004

Lelievre, P. G., & Oldenburg, D. W. (2009). A comprehensive study of linear inverse theory and application to geophysical problems. *Geophysical Journal International, 179*(2), 799–817. https://doi.org/10.1111/j.1365-246X.2009.04334.x

Lelièvre, P. G., Farquharson, C. G., & Hurich, C. A. (2012). Joint inversion of seismic traveltimes and gravity data on unstructured grids with application to mineral exploration. *Geophysics, 77*(1), K1–K15. https://doi.org/10.1190/geo2011-0162.1.

Li, Y., & Oldenburg, D. W. (1996). 3-D inversion of magnetic data. *Geophysics, 61*(2), 394–408. https://doi.org/10.1190/1.1443968.

Li, Y., & Oldenburg, D. W. (1998). 3-D inversion of gravity data. *Geophysics, 63*(1), 109–119. https://doi.org/10.1190/1.1444302.

Li, Y., & Oldenburg, D. W. (2003). Fast inversion of large-scale magnetic data using wavelet transforms and a logarithmic barrier method. *Geophysical Journal International, 152*(2), 251–265. https://doi.org/10.1046/j.1365-246X.2003.01822.

Li, Y., & Shearer, S. E. (2008). Advances in 3D inversion of magnetic data. *The Leading Edge, 27*(1), 64–70. https://doi.org/10.1190/1.2821934

Li, Y., & Shearer, S. E. (2008). Advances in 3D inversion of potential field data in geologically complex environments. *Geophysics, 73*(6), I1–I10. https://doi.org/10.1190/1.2992509

Musa, Y., Ibrahim, A., & Tanko, I. (2023). Geophysical and geological mapping of iron-rich formations in schist-gneiss terrains of Nigeria. *Journal of Geoscience and Environment Protection, 11*(9), 45–62. https://doi.org/10.4236/gep.2023.119004.

Obaje, N. G. (2009). *Geology and mineral resources of Nigeria*. Springer. https://doi.org/10.1007/978-3-540-92685-6

Obi, D. O., Onwuemesi, A. G., Anudu, G. K., Onuba, L. N., & Okonkwo, C. C. (2010). Analysis of aeromagnetic data over Okigwe area, southeastern Nigeria. *Natural Science, 2*(12), 1297–1302. https://doi.org/10.4236/ns.2010.212159

Odeyemi, I. B. (1990). A comparative study of remote sensing images of the structure of the Okemesi fold belt in south-western Nigeria. *Tectonophysics, 173*(1–4), 203–212. https://doi.org/10.1016/0040-1951(90)90221-J.

Odeyemi, I. B., & Afolabi, O. (2014). Lineament fabric and drainage pattern analysis from aeromagnetic data of part of the Basement Complex of southwestern Nigeria. *Journal of Geology and Mining Research, 6*(4), 59–71. https://doi.org/10.5897/JGMR2013.0200.

Odeyemi, I. B., Afolabi, O., & Akinola, O. O. (2012). Application of aeromagnetic data to structural interpretation of Basement Complex rocks in southwestern Nigeria. *Journal of Mining and Geology, 48*(1), 45–56.

Odeyemi, I., & Ibrahim, M. (2024). Geochemistry and tectonic implications of Pan-African granitoids in Nigeria. *Precambrian Research, 392*, 107083. https://doi.org/10.1016/j.precamres.2024.107083.

Ofor, N. P., & Udensi, E. E. (2014). Interpretation of aeromagnetic data over parts of the Bida Basin, Nigeria, using 2D spectral analysis. *International Journal of Basic and Applied Sciences, 3*(3), 19–29.

Ofor, N. P., & Udensi, E. E. (2014). Structural interpretation of the subsurface from aeromagnetic data of parts of Southern Bida Basin, Nigeria. *International Journal of Basic and Applied Sciences, 3*(3), 21–31. https://doi.org/10.14419/ijbas.v3i3.3108

Ogunmola, J. K., Akinlalu, A. A., & Olasunkanmi, N. K. (2020). Aeromagnetic interpretation and 3D inversion modeling of basement structures in the Nigerian schist belt. *Journal of African Earth Sciences, 170*, 103934. https://doi.org/10.1016/j.jafrearsci.2020.103934

Ogunmola, J. K., Ayolabi, E. A., Aizebeokhai, A. P., & Onwuemesi, A. G. (2020). Basement topography and structural analysis of the Middle Benue Trough, Nigeria, using high-resolution aeromagnetic data. *Journal of African Earth Sciences, 162*, 103–716. https://doi.org/10.1016/j.jafrearsci.2019.103716

Ogunmola, J. K., Olatunji, S., & Adelusi, A. O. (2020). Application of aeromagnetic data for subsurface structural mapping and mineral exploration in parts of southwestern Nigeria. *Journal of African Earth Sciences, 167,* 103820. https://doi.org/10.1016/j.jafrearsci.2020.103820

Okonkwo, C. T., & Folorunso, A. F. (2009). Topographic and geological mapping of part of central Nigeria using Shuttle Radar Topography Mission (SRTM) data. *Nigerian Journal of Science, 43*(1), 21–33.

Olade, M. A. (2024). Notes on the nature of lithium mineralization in Nigeria's pegmatite province. *ResearchGate*.

Olawale, S., Usman, R., & Akande, W. (2023). Structural framework and mineralization patterns in schist belts of southwestern Nigeria. *Journal of African Earth Sciences, 201*, 104802. https://doi.org/10.1016/j.jafrearsci.2023.104802.

Onwubuariri, C. N., Nwokoma, E. U., Ezere, U. A., Ugwu, J. U., Onwudo, C. T. (2023) Geophysical Investigation of Environmental and Engineering Features Using Aeromagnetic Data of Ogoja and Environs Southeastern Nigeria. *Nigerian Journal of Physics,* Volume 32(1), 1595-0611

Oyinloye, A. O. (2011). Geology and geotectonic setting of the basement complex rocks in South-Western Nigeria: Implications on provenance and evolution. *Earth Sciences Research Journal*, 15(2), 123–130.

Phillips, S. C., Johnson, J. E., Clyde, W. C., Setera, J. B., Maxbauer, D. P., Severmann, S., & Riedinger, N. (2017). Rock magnetic and geochemical evidence for authigenic magnetite formation via iron reduction in coal-bearing sediments (IODP Site C0020). *Geochemistry, Geophysics, Geosystems*, 18(6), 2076–2098. https://doi.org/10.1002/2017GC006943.

Rahaman, M. A. (1988). Recent advances in the study of the basement complex of Nigeria. In P. O. Oluyide, W. C. Mbonu, A. E. Ogezi, I. G. Egbuniwe, A. C. Ajibade, & A. C. Umeji (Eds.), *Precambrian Geology of Nigeria* (pp. 11–41). Geological Survey of Nigeria.

Salako, K. A. (2014). Basement depth and structural trends in the Upper Benue Trough, NE Nigeria, from aeromagnetic data. *Journal of African Earth Sciences, 96*, 99–109. https://doi.org/10.1016/j.jafrearsci.2014.04.015

Salawu, N. B., & Oden, M. I. (2022). Pan-African tectonics and mineral systems in Nigeria: Implications

for solid mineral exploration. *Ore Geology Reviews, 144,* 104890. https://doi.org/10.1016/j.oregeorev.2022.104890.

Sun, J., & Li, Y. (2014). 3D inversion of magnetic data affected by remanent magnetization. *Geophysics, 79*(1), J1–J11. https://doi.org/10.1190/geo2013-0185.1

Sun, J., & Li, Y. (2014). Adaptive mesh refinement for 3D inversion of magnetic data. *Geophysics, 79*(6), J61–J73. https://doi.org/10.1190/geo2014-0039.1

Udensi, E. E., & Osazuwa, I. B. (2004). Spectral determination of depths to magnetic rocks under the Nupe Basin, Nigeria. *Nigerian Journal of Physics, 16*(2), 91–97.

Utsugi, M. (2021). Magnetic inversion to recover the subsurface block structures based on L1 norm and total variation regularization. *Geophysical Journal International, 228*(1), 510–537. https://doi.org/10.1093/gji/ggab355.

Wang, R., Chen, F., & coauthors. (2024). Prospecting criteria for skarn-type iron deposits in thick overburden areas: implications for remote/indirect detection. *Journal of Applied Geophysics*, 228, 105442. https://doi.org/10.1016/j.jappgeo.2024.105442.

Yakubu, M., Suleiman, M., & Bello, S. (2023). Metamorphic evolution and mineral potential of migmatitic terrains in Nigeria. *Geological Journal, 58*(12), 5124–5143. https://doi.org/10.1002/gj.4821.